Available online at www.CivileJournal.org

Civil Engineering Journal

(E-ISSN: 2476-3055; ISSN: 2676-6957)

Vol. 12, No. 05, May, 2026

Rheological Performance of Asphalt Mastics Incorporating Shale and Pumice as Alternative Mineral Fillers

Suwaphit Chamwon [1], Multazam Hutabarat [1], Preeda Chaturabong [1]*

[1] School of Engineering, King Mongkut's Institute of Technology Ladkrabang, Bangkok 10520, Thailand.

Received 05 February 2026; Revised 21 April 2026; Accepted 28 April 2026; Published 01 May 2026

Abstract

This study investigates the hypothesis that mineral fillers with distinct surface characteristics, mineralogical compositions, and morphologies exhibit different reinforcement mechanisms in asphalt mastics. Shale and pumice were evaluated as alternative mineral fillers and compared with conventional granite and limestone at 20% and 30% filler-to-asphalt (F/A) ratios by volume. Filler characterization included X-ray diffraction (XRD) analysis, scanning electron microscopy (SEM), specific surface area (SSA), and hydrophilicity coefficient (HC) measurements. Rheological characterization was performed using dynamic shear rheometer, including temperature sweep, frequency sweep master curves, multiple stress creep recovery (MSCR), linear amplitude sweep (LAS), and Glover–Rowe (G–R) analyses. Pumice, dominated by amorphous volcanic glass with the highest SSA (59.18 m²/g), exhibited rutting-dominant modification with the highest complex modulus enhancement (7.3–9.4 times at 30% F/A) and lowest non-recoverable creep compliance. Shale, composed primarily of quartz and kaolinite with layered morphology and moderate SSA (43.00 m²/g), demonstrated balanced rheological response and achieved the longest fatigue life (Nf,5% = 45,200 cycles at 20% F/A). These findings demonstrate that filler-specific reinforcement mechanisms are governed by mineralogical composition and morphology, supporting performance-based filler selection tailored to climatic and loading conditions.

Keywords: Asphalt Mastic; Rheology; Mineral Filler; XRD; Rutting Resistance; Fatigue Life; Performance-Based Selection.

1. Introduction

The long-term performance of asphalt pavements depends fundamentally on the complex interactions between asphalt binder, mineral aggregates, and fine fillers. Asphalt mastic (the blend of asphalt binder and mineral filler) serves as the critical binding phase governing rheological response and mechanical behavior [1–3]. Filler–binder interaction directly influences viscosity, stiffness, and resistance to permanent deformation [4, 5].

The physical characteristics of filler particles “including particle size distribution, specific surface area (SSA), and morphology” exert greater influence on mastic stiffness than mineralogical composition alone [6–8]. However, recent studies have demonstrated that mineralogical composition, as characterized by X-ray diffraction (XRD), plays a complementary role by governing surface chemistry and the nature of physico-chemical interactions at the filler–binder interface [9, 10]. Traditional empirical tests have confirmed that mineral filler incorporation enhances stiffness and hardness [11, 12], with fundamental mechanisms clarified through mastic-scale studies [13, 14].

At the microscale, mineral filler particles trigger interfacial phenomena that alter the binder structure. As proposed by Tan & Guo [13] (Figure 1), chemical components undergo spatial rearrangement near filler surfaces, forming a

---

* Corresponding author: preeda.ch@kmitl.ac.th

https://doi.org/10.28991/CEJ-2026-012-05-020

diffusion–solvation membrane that creates a thin "structural asphalt binder" layer with elevated viscosity adjacent to the filler, and an outer "free asphalt binder" region retaining bulk properties. As filler content increases, the structural fraction grows, reducing fluidity while enhancing reinforcement [14].

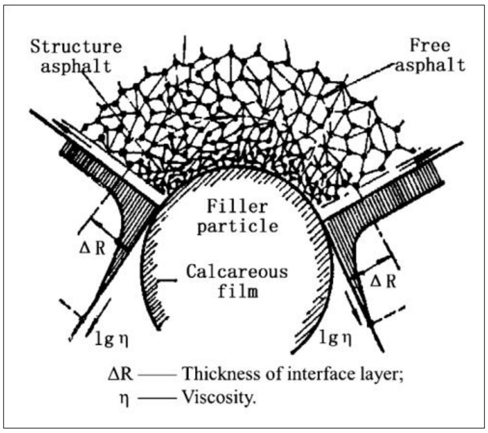

Figure 1. The interaction model between asphalt binder and mineral filler [13]

Dynamic shear rheometer (DSR) testing enables evaluation of complex modulus (|G*|), phase angle (δ), rutting resistance, fatigue behavior, and cracking susceptibility [15]. Increasing filler volume fraction leads to higher |G*| and rutting factor (|G*|/sin δ) [16-18], attributed to enhanced surface energy and binder adsorption [19]. However, stiffening often accompanies reduced fatigue resistance, as demonstrated by VECD modeling and LAS testing [20, 21], highlighting the necessity of balancing rutting and fatigue performance [21, 22].

Despite this understanding, mineral filler selection remains largely prescriptive. Conventional fillers (granite, basalt, limestone) dominate due to availability and historical performance [23]. Increasing emphasis on sustainability and application-specific performance has driven interest in alternative fillers [24–26], but existing literature provides limited insight into how surface characteristics, mineralogical composition, and morphology govern mastic-level mechanisms.

Among alternative fillers, pumice and shale represent materials with fundamentally different characteristics. Pumice is a lightweight volcanic rock with high porosity, low density, and large SSA [27], showing favorable moisture resistance [28] and improved high-temperature performance [29–31]. Shale is a fine-grained sedimentary rock exhibiting lamellar structure and moderate surface activity [32–34]. Both are locally available in Thailand from construction and mining stockpiles, providing sustainable alternatives where limestone is limited.

The mechanistic link between filler morphology and rheological reinforcement operates through binder adsorption capacity and interfacial stress distribution. Porous fillers promote extensive adsorption, creating thick interfacial layers that increase stiffness—favorable for rutting resistance. Layered fillers distribute stresses across parallel planes, facilitating stress relaxation—conducive to fatigue performance [5, 8, 35]. However, the combined influence on performance-based behavior remains insufficiently clarified for non-conventional fillers, particularly when mineralogical differences are considered.

Accordingly, this study hypothesizes that mineral fillers with distinct mineralogical compositions and morphologies exhibit different reinforcement mechanisms. Fillers with porous, amorphous structure and extensive binder adsorption are expected to preferentially enhance rutting resistance, whereas fillers with layered clay mineral content and moderate surface activity are anticipated to promote balanced viscoelastic response and improved fatigue performance. To test this hypothesis, comprehensive physical, mineralogical, and rheological characterization was conducted comparing shale and pumice against granite and limestone at two F/A ratios.

2. Materials and Methods

2.1. Materials Selection and Properties

The study utilizes four mineral fillers: two conventional (granite and limestone) and two alternatives (shale and pumice), as shown in Figure 2. Conventional fillers were sourced from Rong Mo Hin Granite Tak Co., Ltd. Shale and pumice were obtained from local stockpiles in Thailand, selected based on: (i) their distinct physical properties—pumice representing porous, high-SSA morphology and shale representing layered, moderate-SSA morphology—providing contrasting cases for investigating morphology–performance relationships; and (ii) regional availability and economic viability as alternatives to conventional fillers.

Figure 2. Mineral fillers used in this study

Physical properties were determined using standardized procedures: density (ASTM D854), SSA (BET method with nitrogen adsorption), hydrophilicity coefficient (HC) following Zhao et al. [11], and particle size distribution (Malvern Mastersizer 3000). Microstructure was characterized using scanning electron microscopy (SEM). Results are summarized in Table 1 and Figure 3.

Table 1. Properties of mineral fillers.

Properties	Granite	Limestone	Shale	Pumice
Density (g/cm^3)	2.50	2.66	2.70	2.41
SSA (m^2/g)	32.79	34.38	43.00	59.18
HC	0.80	0.83	0.68	0.63

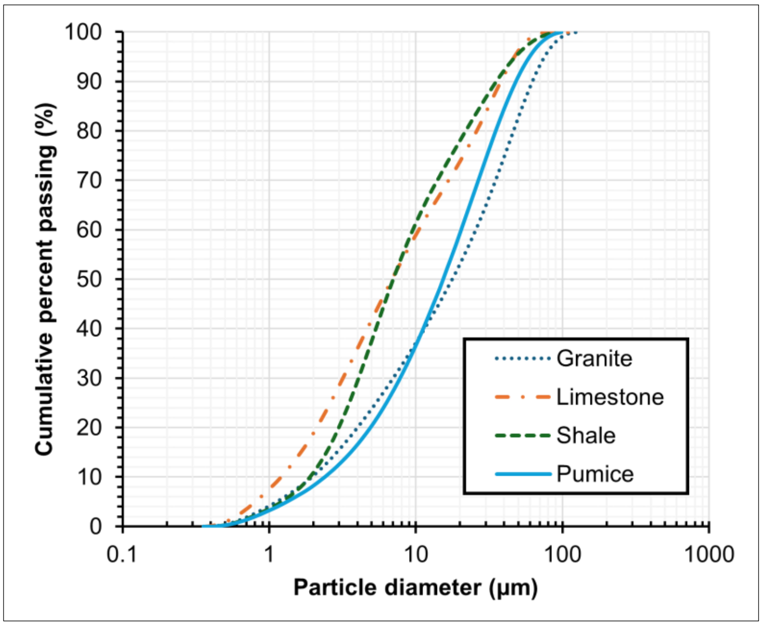

Figure 3. Mineral filler particle size distribution

The particle size distributions (Figure 3) reveal that limestone and shale exhibit comparable distributions with predominantly fine particles, whereas granite and pumice show coarser sizes with similar distributions. Finer particles (limestone, shale) provide greater packing efficiency, potentially reducing inter-particle voids and enhancing binder film uniformity. In the case of pumice, coarser particle size is compensated by substantially higher SSA due to internal porosity. The combination of particle size and SSA determines the effective filler–binder contact area, governing the extent of structural asphalt binder formation [6, 35].

2.2. Mineralogical Characterization (XRD)

To provide deeper insight into the mineralogical composition and its role in filler–binder interaction mechanisms, X-ray diffraction (XRD) analysis was performed on all four mineral fillers. XRD patterns were obtained using a diffractometer with Cu Kα (λ = 1.5406 Å) over a 2θ range of 10–80°. The identified mineral phases and their implications for filler–binder interaction are presented in Figure 4 and summarized in Table 2.

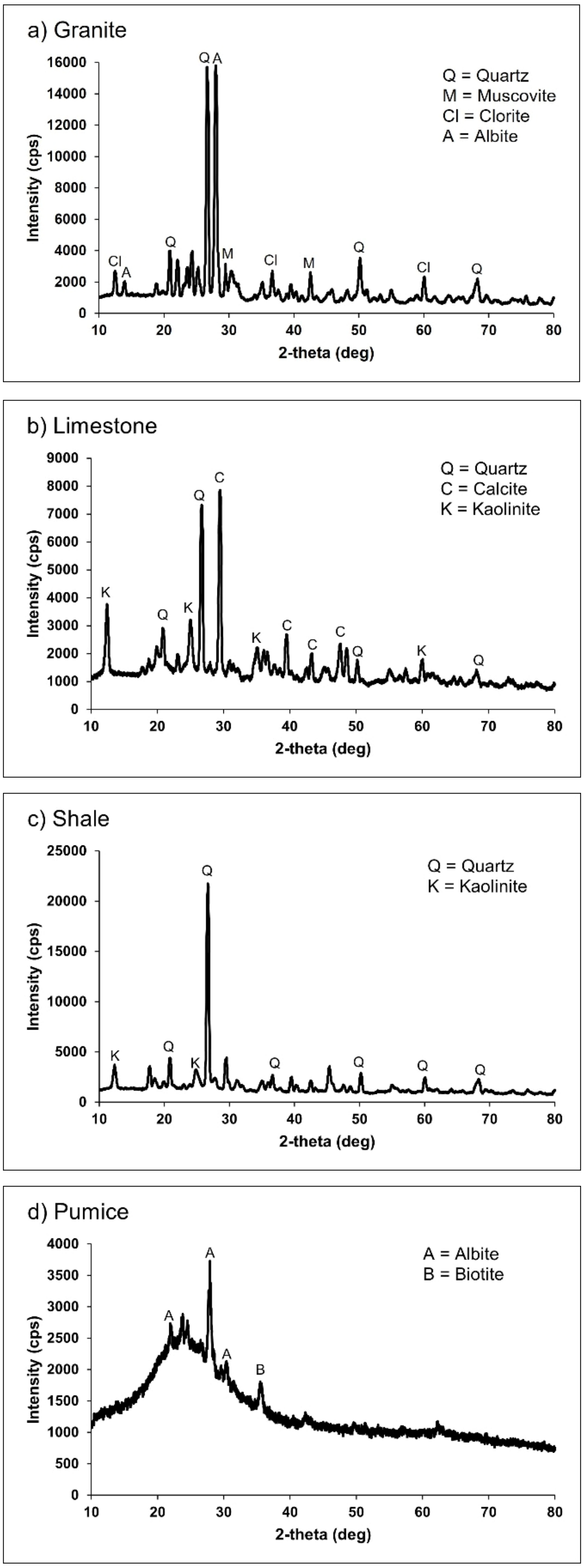

Figure 4. XRD patterns of mineral fillers: (a) granite; (b) limestone; (c) shale; (d) pumice

Table 2. Summary of mineralogical composition from XRD analysis.

Filler	Dominant Phases	Secondary Phases	Structural Character
Granite	Quartz, Albite	Muscovite, Chlorite	Highly crystalline
Limestone	Calcite, Quartz	Kaolinite	Crystalline (carbonate)
Shale	Quartz	Kaolinite	Crystalline + clay layers
Pumice	Amorphous glass	Albite, Biotite	Predominantly amorphous

The XRD results (Figure 4) reveal distinct mineralogical characteristics among the four fillers that provide critical context for interpreting their rheological behavior:

Granite (Figure 4-a) exhibited sharp, well-defined diffraction peaks dominated by quartz ($2\theta \approx 20.9^\circ$, 26.6º, 50.1º, 68.1º) and albite ($2\theta \approx 27.9^\circ$), with secondary peaks of muscovite ($2\theta \approx 29.9^\circ$, 45.2º) and chlorite ($2\theta \approx 12.5^\circ$, 38.5º, 60.8º). The highly crystalline silicate framework explains granite's angular, polygonal SEM morphology (Figure 4-a) and its relatively low SSA (32.79 m^2/g), as the well-ordered crystal surfaces provide limited adsorption sites for binder molecules.

Limestone (Figure 4-b) was dominated by calcite ($2\theta \approx 29.4^\circ$, 39.4º, 43.2º, 47.5º), with secondary quartz ($2\theta \approx 20.9^\circ$, 26.6º, 50.1º, 68.1º) and kaolinite ($2\theta \approx 12.3^\circ$, 24.9º, 62.3º). The carbonate-dominant mineralogy is significant because calcite surfaces are inherently more hydrophilic than silicate surfaces, which explains limestone's highest HC value (0.83) and consequently its lower chemical compatibility with the non-polar asphalt binder components.

Shale (Figure 4-c) displayed a quartz-dominant pattern ($2\theta \approx 26.6^\circ$) with prominent kaolinite peaks ($2\theta \approx 12.3^\circ$, 24.9º). The identification of kaolinite—a layered aluminosilicate clay mineral—is particularly significant as it directly explains the lamellar morphology observed in SEM (Figure 4-c). Kaolinite's characteristic 1:1 layered structure (alternating tetrahedral silica and octahedral alumina sheets) provides: (i) the planar, sheet-like particle geometry that enables microscale stress distribution across multiple planes, and (ii) moderate surface hydroxyl groups that facilitate balanced adhesion with asphalt binder components without excessive adsorption (HC = 0.68). This mineralogical evidence provides a mechanistic basis for shale's hypothesized balanced rheological behavior.

Pumice (Figure 4-d) exhibited a fundamentally different diffraction pattern characterized by a broad amorphous hump centered between 20 – 30º 2θ, with only minor crystalline peaks attributable to albite ($2\theta \approx 22.0^\circ$, 27.9º, 30.3º) and biotite ($2\theta \approx 35.0^\circ$). The predominantly amorphous character indicates that pumice is composed mainly of volcanic glass—a disordered silicate network formed during rapid lava quenching. This amorphous structure has several important implications: (i) the disordered atomic arrangement creates extensive internal porosity and surface irregularity, directly accounting for pumice's exceptionally high SSA (59.18 m^2/g) despite its relatively coarse particle size; (ii) the amorphous silicate surface provides abundant reactive sites (non-bridging oxygen atoms and silanol groups) that promote strong adsorption of polar binder fractions; and (iii) the low HC (0.63) reflects the lipophilic character of the amorphous glass surface. These mineralogical characteristics provide the mechanistic foundation for pumice's expected rutting-dominant modification behavior.

A penetration-grade asphalt binder (AC 60/70) produced by TIPCO in Thailand was used. Key properties are summarized in Table 3.

Table 3. Properties of the asphalt binder

Properties	Method	Results
Penetration (0.1 mm) at 25 °C	ASTM D5	64
Softening point (°C)	ASTM D36	48.8
Ductility (cm) at 5 °C	ASTM D113	150 +
Flash point (°C)	ASTM D92	346
Density at 15 °C (g/m3)	ASTM D70	1.0332
Dynamic shear, $\|G^*\|/\sin\delta$ at 64 °C (kPa)	AASHTO T315	1.28

2.3. Mastic Preparation

Asphalt mastics were prepared by blending asphalt binder with mineral fillers at two F/A ratios by volume: 20% and 30%. Higher concentrations were avoided to minimize particle-to-particle contact effects dominating above 40% [36]. The procedure involved: (i) drying fillers at 110 °C for 24 hours; (ii) heating binder to 160 °C for two hours; (iii) gradual addition with manual mixing for five minutes; and (iv) blending at 2000 rpm for 30 minutes using an overhead stirrer (IKA-RW20) at 160 °C.

Noticeable workability difficulties were observed at the 30% F/A ratio for pumice. The high SSA (59.18 m^2/g) results in extensive binder adsorption, substantially increasing viscosity and reducing workability. For field implementation, pumice-modified mastics at high F/A ratios may require adjusted mixing temperatures, extended blending times, or warm-mix additives. Preliminary workability trials are recommended to determine the maximum feasible pumice F/A ratio, maintaining both laboratory performance and field compactability. Sample designations are presented in Table 4.

Table 4. Sample symbols of Asphalt mastic.

Mastic Composition	20% F/A	30% F/A
Granite	G20	G30
Limestone	L20	L30
Shale	S20	S30
Pumice	P20	P30

2.4. Rheological Testing Methods

The experimental workflow is presented in Figure 5. All rheological characterization used a DSR (SmartPave 102, Anton Paar, Austria) following EN 14770. The program comprised temperature sweep, frequency sweep, MSCR, LAS, and G–R analyses. A 25 mm plate/1 mm gap was used for 40–80 °C and 8 mm plate/2 mm gap for 5–40 °C. All tests were performed in triplicate. Standard deviations were calculated for all measurements. The coefficient of variation (COV) for |G*| was generally below 8%.

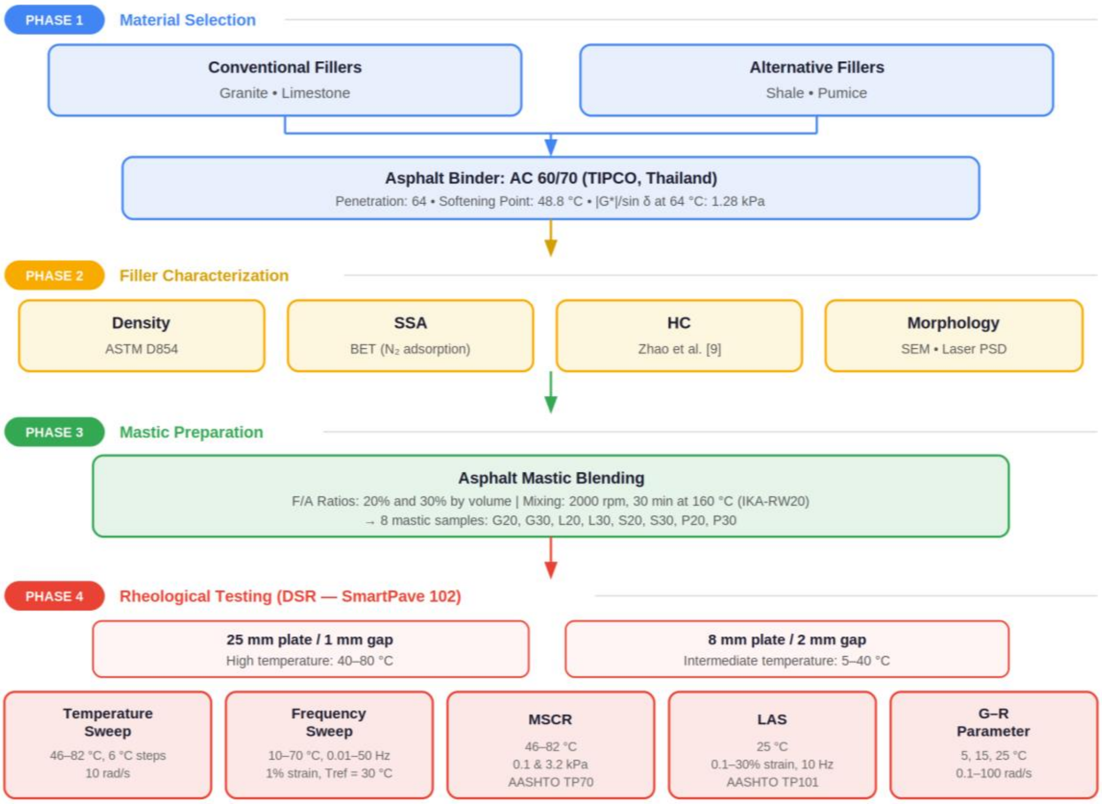

Figure 5. Flowchart of the experimental methodology

2.4.1. Temperature Sweep Test

Testing followed AASHTO T 315-06 at 46–82 °C in 6 °C increments at 10 rad/s. The complex modulus (|G*|, ratio of peak shear stress to peak shear strain under sinusoidal loading) and phase angle (δ, lag between stress and strain where 0° = purely elastic, 90° = purely viscous) were measured.

2.4.2. Frequency Sweep and Master Curves

Frequency sweep tests were performed to characterize the rate-dependent behavior of asphalt mastics across a range of temperatures and loading frequencies relevant to field conditions. Tests were conducted at seven temperatures (10-70°C at 10°C intervals) over a frequency range of 0.01-50 Hz. A controlled strain amplitude of 1% was applied to maintain testing within the linear viscoelastic regime, ensuring that material response remained independent of strain magnitude. The resulting data were analyzed using the Time-Temperature Superposition Principle (TTSP) to construct master curves at a reference temperature of 30°C. TTSP exploits the fundamental equivalence between temperature and loading rate in viscoelastic materials: the effect of increasing temperature is equivalent to decreasing the loading rate, and vice versa. As temperature increases, the complex modulus decreases and the entire modulus-frequency curve shifts to lower frequencies without changing its fundamental shape [37]. This behavior allows data collected at multiple temperatures to be horizontally shifted along the frequency axis and superimposed into a single master curve, effectively extending the observable frequency range by several orders of magnitude.

The master curve construction process involves determining temperature-dependent shift factors (aT) that align isothermal data sets. These shift factors quantify how much each temperature curve must be shifted to overlap with the reference temperature data. The resulting master curve is typically fitted with a sigmoidal function (Equation 1) [38], which provides a smooth mathematical representation of the material's stiffness across the extended frequency range:

$$\log G^* = \partial + \frac{\alpha}{1+e^{\beta+\gamma(\log f_r)}} \tag{1}$$

where, ∂ denoting the lower asymptote, α is the difference between the upper and lower asymptote values, β and γ defining the shape between the asymptotes and the location of the inflection point and log (f_r) represents the log reduced frequency. The mathematical expression for f_r is the result of applying the principle of time– temperature correspondence to the real frequency using shift factors as shown in Equation 2:

$$a_T = \frac{f_r}{f} \tag{2}$$

The temperature shift factor (a_T) in the TTSP is identified using the classical Williams-Landel-Ferry (WLF) nonlinear equation as shown in Equation 3:

$$\log a_T = \frac{-C_1(T-T_{ref})}{C_2(T-T_{ref})} \tag{3}$$

where, T is the loading temperature in the tests and T_{ref} is the reference temperature, C_1 and C_2 are material constants.

2.4.3. Multiple Stress Creep Recovery (MSCR)

The MSCR test was conducted following AASHTO TP70 protocols to assess rutting resistance under conditions that more closely simulate actual pavement loading than traditional oscillatory testing. Unlike sinusoidal loading, MSCR applies sustained creep stress followed by unloaded recovery periods, mimicking the behavior of asphalt under slow-moving or stationary traffic. The test protocol consisted of two stress levels applied sequentially. First, 10 creep-recovery cycles were performed at 0.1 kPa stress (representing light traffic conditions), with each cycle comprising 1 second of loading followed by 9 seconds of recovery. The stress was then increased to 3.2 kPa for an additional 10 cycles to simulate heavy truck loading. From the resulting creep and recovery curves, two critical parameters were extracted: non-recoverable creep compliance (Jnr), which quantifies the material's susceptibility to permanent deformation, and percent recovery (%R), which measures the elastic recovery after load removal. Lower Jnr values and higher %R indicate better rutting resistance. To capture performance across the full range of high pavement temperatures, tests were conducted at seven temperatures spanning 46-82°C in 6°C increments. This temperature range encompasses typical summer pavement conditions in tropical and subtropical climates where rutting is most problematic.

2.4.4. Linear Amplitude Sweep (LAS)

The Linear Amplitude Sweep (LAS) test evaluated fatigue resistance through a two-stage protocol. First, a frequency sweep (0.2–30 Hz) at 0.1% strain amplitude characterized the undamaged material response and established the storage modulus-frequency relationship. Subsequently, the amplitude sweep progressively increased strain from 0.1% to 30% at a constant frequency of 10 Hz. Failure was defined using the viscoelastic continuum damage (VECD) criterion as a 35% reduction in the integrity parameter $|G^*| \cdot \sin\delta$. Fatigue life (N_f) at specified strain levels was calculated according to Equation 4

$$N_f = A_{35}(\gamma_{max})^{-B} \tag{4}$$

where, γ_{max} is the peak strain amplitude, A_{35} and B are the viscoelastic continuum damage (VECD) coefficients. The experiment was conducted at a temperature of 25°C. The LAS test result was used to calculate the fatigue life at varying strain levels of 2.5% and 5% in accordance with the standard recommended in AASHTO TP101 [39].

2.4.5. Glover–Rowe (G–R) Parameter

The Glover-Rowe (G-R) parameter is a valuable tool for assessing the cracking resistance of asphalt binders based on their complex modulus and phase angle at low temperatures. The G-R parameter for asphalt binder can be computed using the complex modulus and phase angle at a frequency of 0.005 rad/s and temperature of 15 °C, as shown in Equation 5 [40].

$$G - R = \frac{G^*(\cos\delta)^2}{\sin\delta} \tag{5}$$

Furthermore, one method to obtain the G-R parameter is to construct the master curve using the time-temperature principle with 15°C as the reference temperature to calculate the G-R parameter, which is carried out by a frequency sweep test on the asphalt binder and mastics at three different temperatures: 5°C, 15°C, and 25°C and a frequency range of 0.1–100 rad/s [41].

3. Results and Discussion

3.1. Physical Properties of Mineral Filler

The physical properties (Table 1) and mineralogical compositions (Table 2, Figure 4) together provide a comprehensive framework for understanding filler–binder interaction. Shale exhibited the highest density (2.70 g/cm³) while pumice showed the lowest (2.41 g/cm³). SSA was highest for pumice (59.18 m²/g), followed by shale (43.00 m²/g), limestone (34.38 m²/g), and granite (32.79 m²/g). The HC was lowest for pumice (0.63) and shale (0.68), indicating stronger lipophilic properties.

The XRD analysis reveals that these physical property differences are fundamentally governed by mineralogical composition. Pumice's exceptionally high SSA, despite its relatively coarse particle size, is explained by its predominantly amorphous volcanic glass structure (Figure 6d), which creates extensive internal porosity and surface irregularity. In contrast, granite's low SSA corresponds to its highly crystalline quartz–albite framework (Figure 6a), where well-ordered crystal faces provide limited adsorption sites. Limestone's highest HC (0.83) is directly attributable to its calcite-dominant mineralogy (Figure 6b), as carbonate surfaces exhibit greater hydrophilicity than silicate surfaces. Shale's moderate SSA and HC are consistent with its quartz–kaolinite composition (Figure 6c), where the layered clay mineral provides moderate surface hydroxyl groups for balanced adhesion.

The SEM micrographs (Figure 6) corroborate the XRD findings. Granite's angular, polygonal shapes reflect its crystalline silicate framework. Limestone's lamellar structure corresponds to calcite's rhombohedral cleavage. Shale's layered morphology directly corresponds to kaolinite's sheet structure. Pumice's polygonal shapes with visible internal porosity reflect the vesicular nature of amorphous volcanic glass. This convergent evidence from XRD and SEM establishes a clear mineralogy–morphology–surface property relationship that underpins the rheological behavior of the resulting mastics.

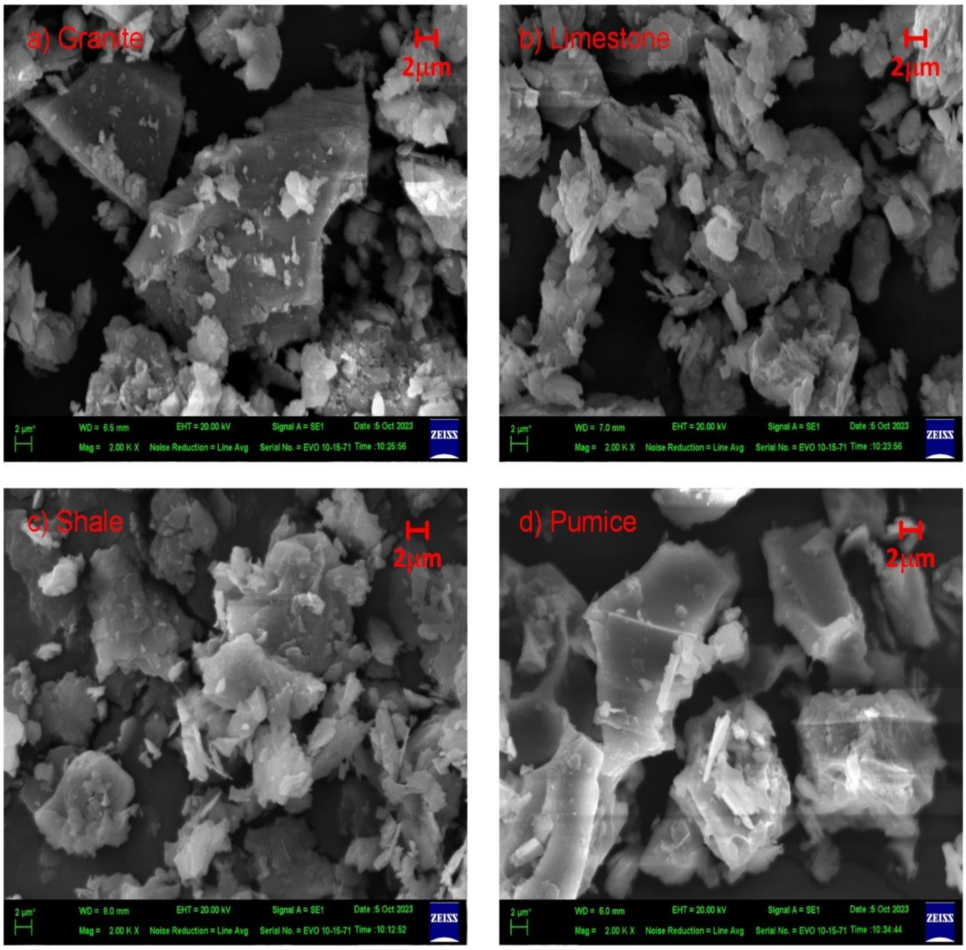

Figure 6. SEM morphology: (a) granite; (b) limestone; (c) shale; (d) pumice

3.2. Complex Modulus and Phase Angle

The isothermal plots (Figures 7 and 8) demonstrate that filler incorporation substantially increased stiffness, with pumice exhibiting the highest |G*|, followed by shale, limestone, and granite. This ranking corresponds directly to the SSA ranking and can now be mechanistically linked to mineralogical composition: pumice's amorphous glass structure provides abundant reactive surface sites for binder adsorption, while granite's crystalline quartz–albite framework offers limited adsorption capacity [13, 42].

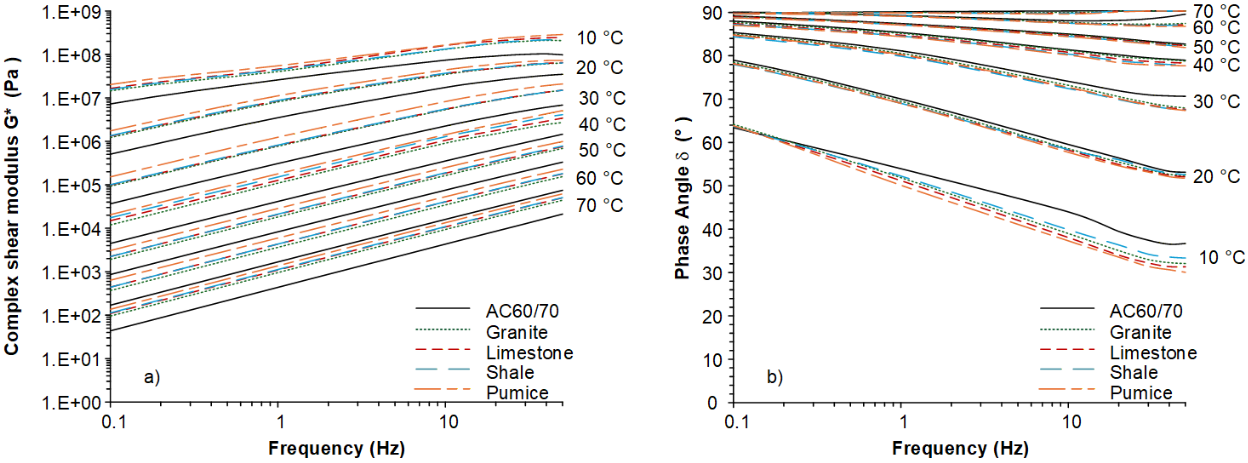

Figure 7. Isothermal plots at 20% F/A ratio

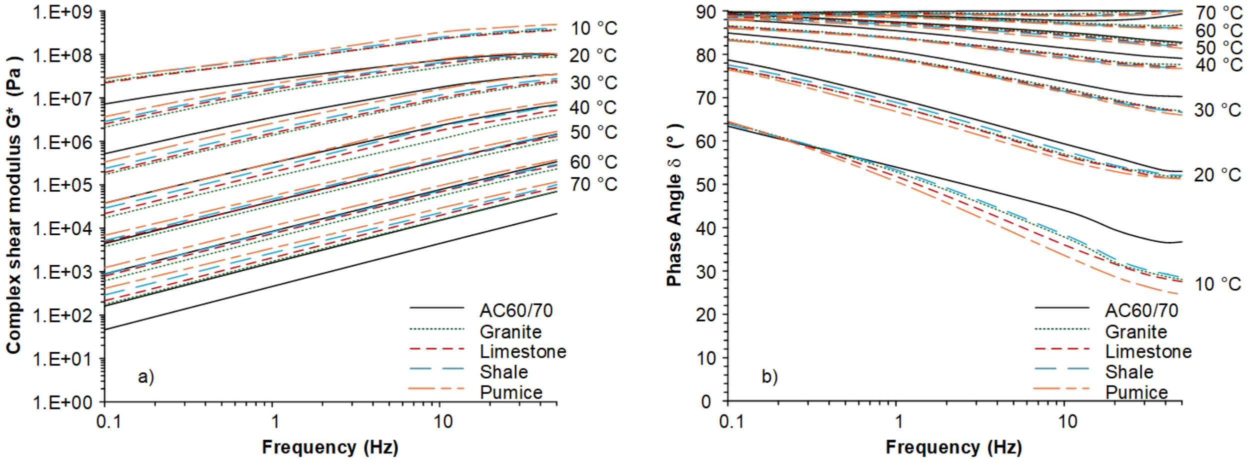

Figure 8. Isothermal plots at 30% F/A ratio

Phase angle results reveal temperature-dependent differences that reflect filler-specific reinforcement mechanisms. At 10–20 °C, shale exhibited the highest δ, while pumice had the lowest. Above 20 °C, granite showed the most viscous behavior. Pumice's amorphous glass surface creates extensive, strongly bonded interfacial layers effective across all temperatures, whereas granite's crystalline surfaces provide weaker bonding with greater temperature sensitivity (see Figure 9).

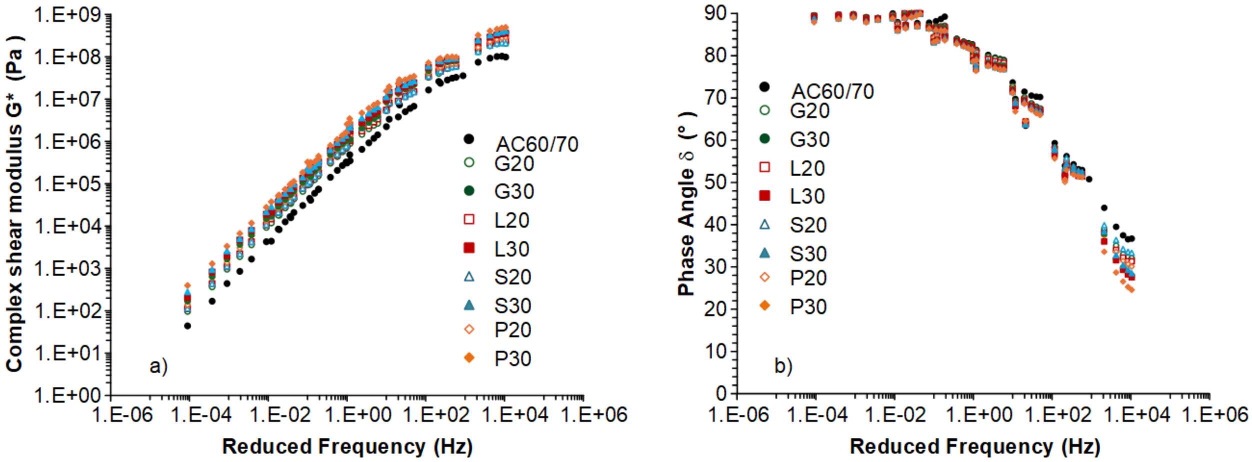

Figure 9. Master curves at T_{ref} = 30 °C

At 30% F/A, pumice produced stiffness ratios of 7.3–9.4 times (50–70 °C), while granite achieved only 2.30–2.48 times (see Figure 10). Since all fillers were at identical volume fractions, this difference cannot be explained by packing alone. The XRD evidence supports an adsorption-driven mechanism: pumice's amorphous glass provides ~1.8 times more surface area per unit mass than granite, and its disordered silicate network contains abundant non-bridging oxygen atoms that serve as preferential adsorption sites for polar asphaltene molecules [9, 13, 14].

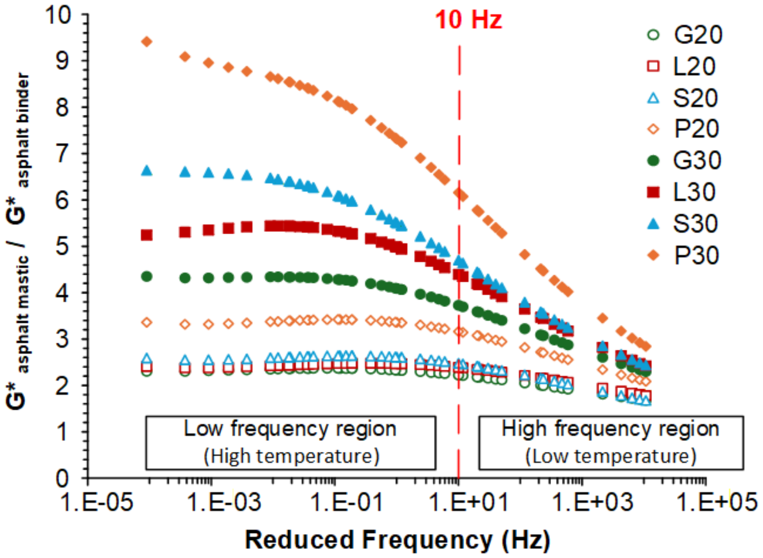

Figure 10. Mastic-to-binder stiffness ratio vs. reduced frequency

3.3. High-Temperature Rheological Properties

3.3.1. Temperature Sweep Test

Temperature sweep results (Figure 11) confirm pumice-filled mastics exhibited the highest |G*| and rutting factor values, followed by shale, limestone, and granite. All mastics exceeded the Superpave threshold (1.0 kPa). The mineralogical basis for pumice's superior rutting resistance lies in its amorphous glass structure, which maximizes binder adsorption and creates extensive interfacial reinforcement that restricts viscous flow under sustained loading [19, 23].

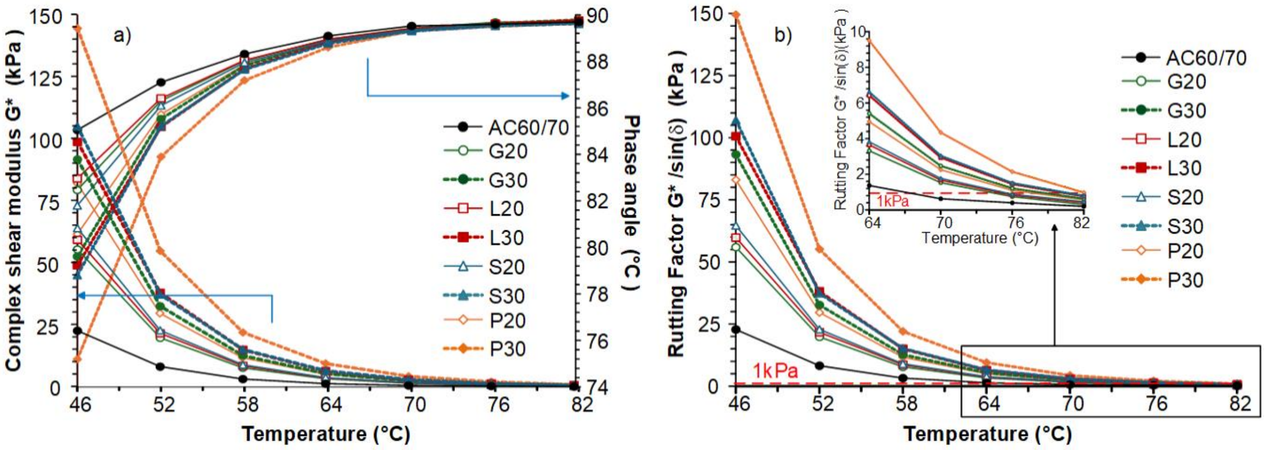

Figure 11. Temperature sweep: (a) |G*| and δ; (b) rutting factor

3.3.2. MSCR Test

MSCR results (Figures 12 to 14) provide realistic rutting assessment. Granite demonstrated the highest cumulative strain, while pumice exhibited the lowest.

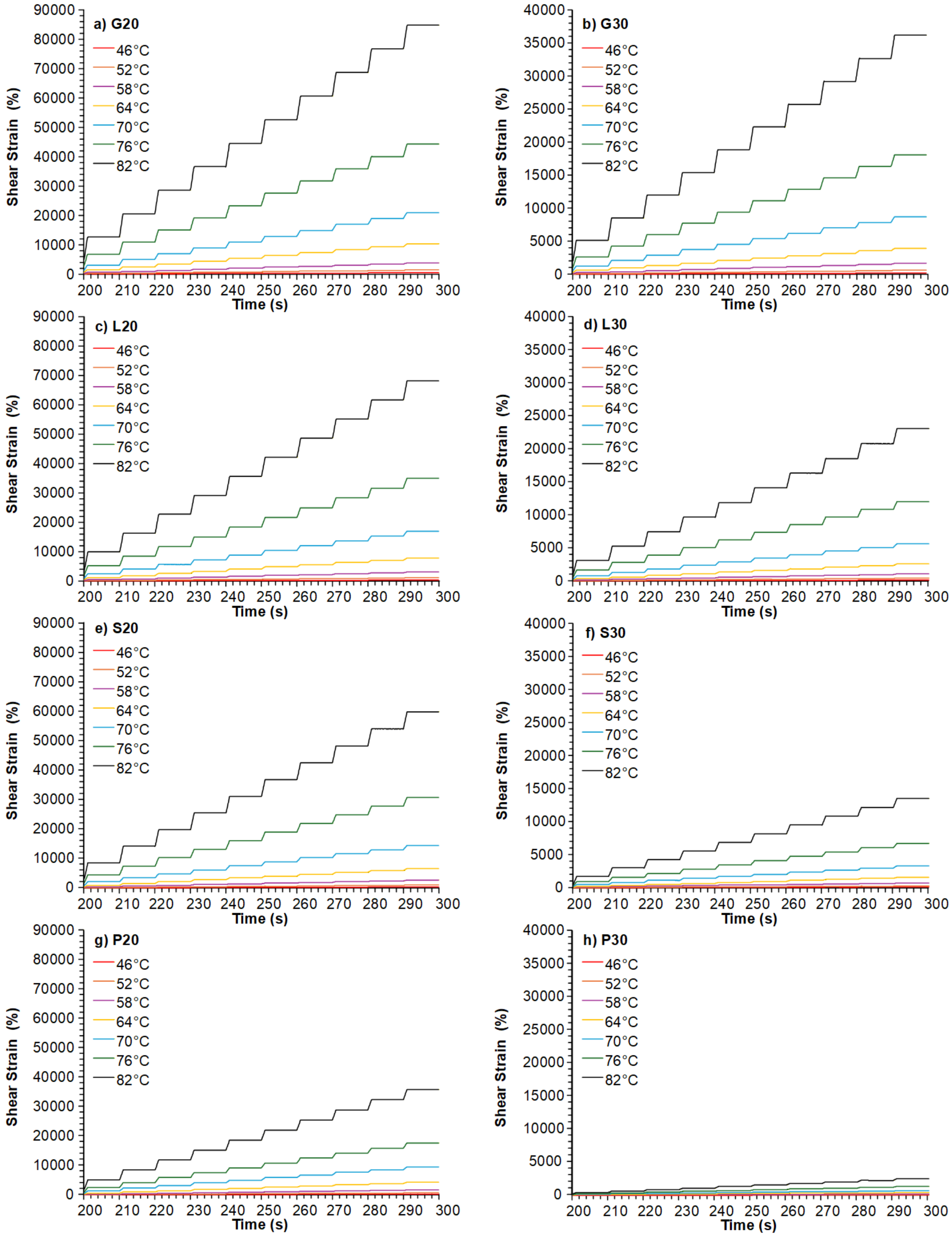

Figure 12. Shear strain curves

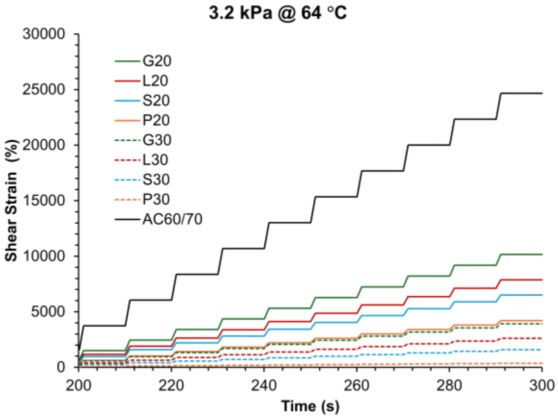

Figure 13. Shear strain curves at 64 °C

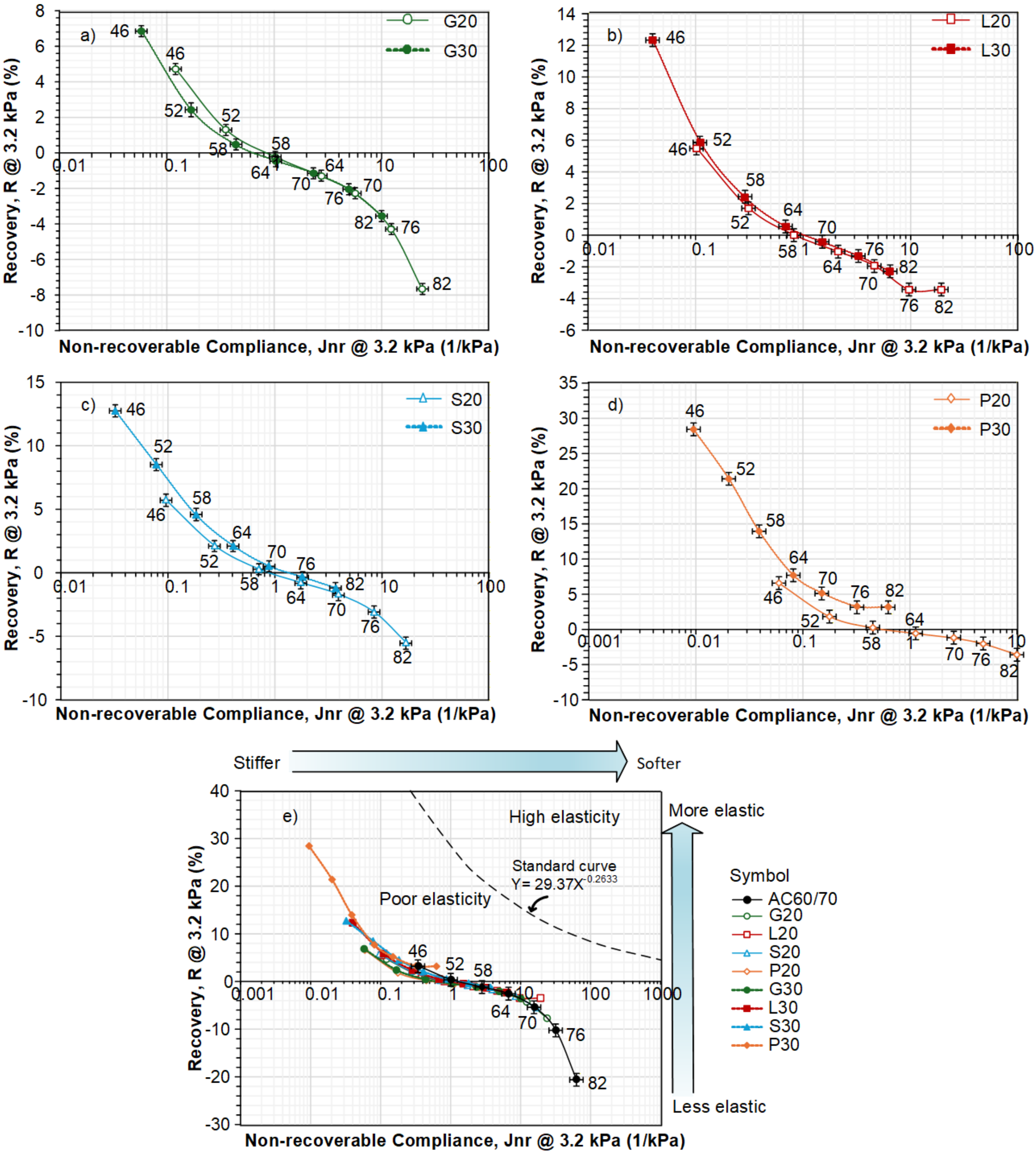

Figure 14. MSCR results: (a) Jnr; (b) percent recovery

Pumice reduced Jnr by 83.62% and 98.53% at 20% and 30% F/A respectively, followed by shale (73.74%, 93.32%), limestone (69.85%, 89.59%), and granite (62.97%, 84.17%). Pumice's 98.53% reduction exceeds values reported for most conventional and alternative fillers [16, 18, 21]. Notably, pumice at 20% F/A achieved rutting resistance comparable to granite at 30% F/A.

The mineralogical explanation for this performance hierarchy is now clear: pumice's amorphous glass creates the most extensive structural binder layer through reactive surface adsorption; shale's kaolinite provides moderate but effective clay–binder interaction; limestone's hydrophilic calcite surface limits binder immobilization; and granite's crystalline quartz–albite framework offers the least adsorption capacity. The percent recovery results further confirm this: pumice demonstrated measurable strain recovery up to 82 °C, indicating that the adsorption-driven structural layers maintain elasticity to higher temperatures [13, 42].

3.4. Intermediate Temperature Rheological Properties

The LAS test results (Figure 15) show shear stress initially increases linearly with strain before declining, indicating progressive damage. Pumice-filled mastics achieved the highest peak shear stress due to greater stiffness. The damage characteristic curves (Figure 16) confirm that pumice reached failure at lower damage intensity, demonstrating the inverse stiffness–damage tolerance relationship [20, 43]. Fatigue life results (Figure 17) reveal hierarchical patterns supporting the hypothesis.

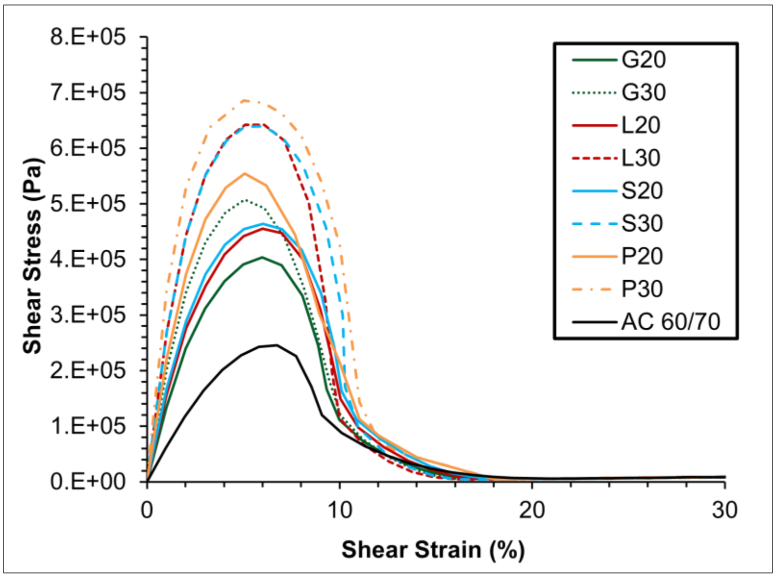

Figure 15. LAS stress–strain curves

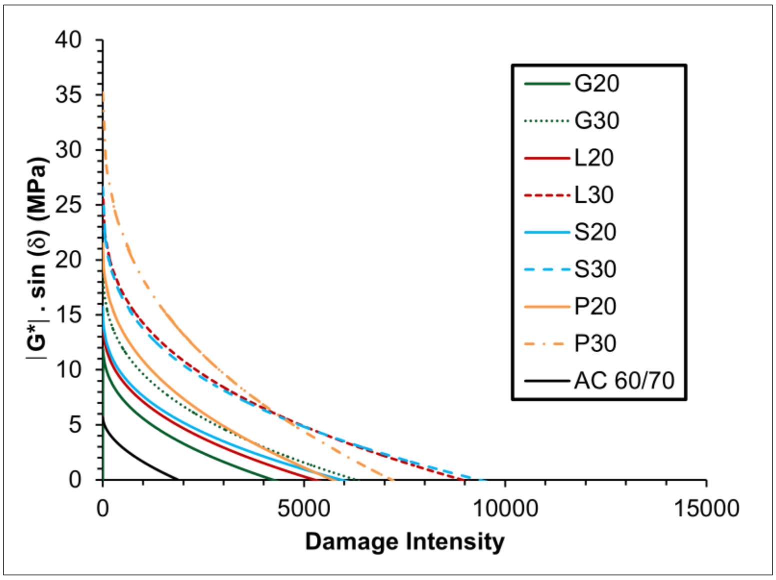

Figure 16. Damage characteristic curves

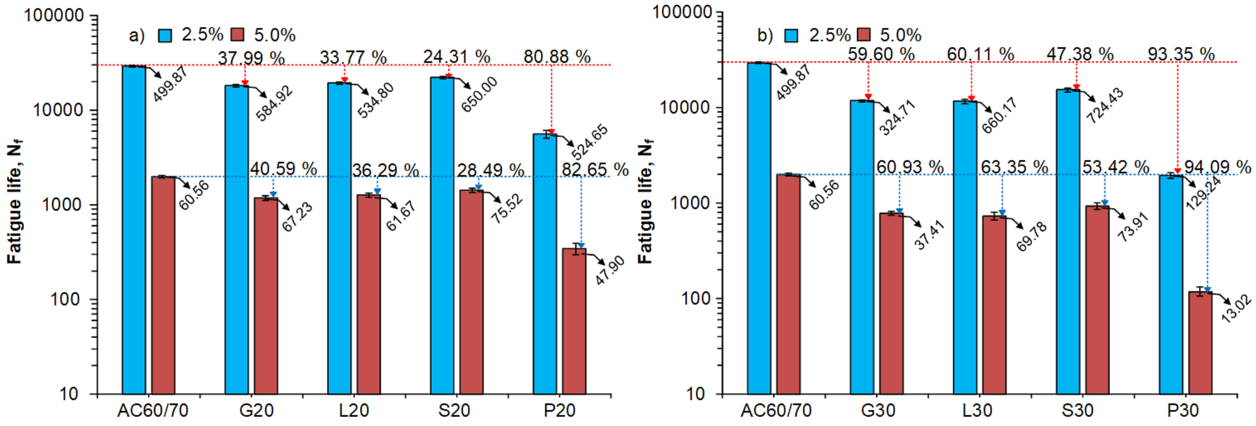

Figure 17. Fatigue life at (a) 2.5% and (b) 5% strain

All fillers reduced fatigue life vs. neat binder (28.49% for S20 to 63.35% for L30 at 5% strain). Among fillers, shale achieved the longest fatigue life (Nf,5% = 45,200 cycles at 20% F/A), followed by limestone and granite (37,500–39,800 cycles), while pumice showed the shortest (29,300 cycles at 20% F/A) despite highest rutting resistance.

The XRD evidence provides a clear mineralogical explanation for shale's superior fatigue performance. The presence of kaolinite—a 1:1 layered aluminosilicate clay mineral—creates a particle morphology with parallel sheet structures that enable microscale stress relaxation across multiple planes. Under cyclic loading, the kaolinite layers can accommodate shear deformation through interlayer sliding without catastrophic failure, while the moderate surface hydroxyl content provides adequate but not excessive binder adhesion (HC = 0.68). This contrasts sharply with pumice, whose amorphous glass creates rigid, strongly bonded interfacial structures that concentrate cyclic stress rather than dissipating it, leading to accelerated fatigue damage despite higher initial stiffness.

This mineralogy–performance relationship is consistent with Grabowski & Wilanowicz [44] and Chaudhary et al. [21]. The inverse rutting–fatigue relationship suggests climate-specific optimization: pumice for hot climates (>30 °C) where rutting dominates; shale for moderate climates with thermal cycling where both distresses are relevant.

3.5. Glover-Rowe Parameter Analysis

G–R results (Figure 18) show all materials below the warning threshold (G–R < 180 kPa). Shale exhibited the highest values (98–145 kPa), followed by pumice (85–132 kPa), limestone (72–108 kPa), and granite (65–95 kPa). The aging trajectory of these fillers may differ due to their distinct mineralogies: pumice's amorphous glass may sequester reactive binder components, while limestone's calcite could catalyze oxidation [9, 10]. This warrants future investigation.

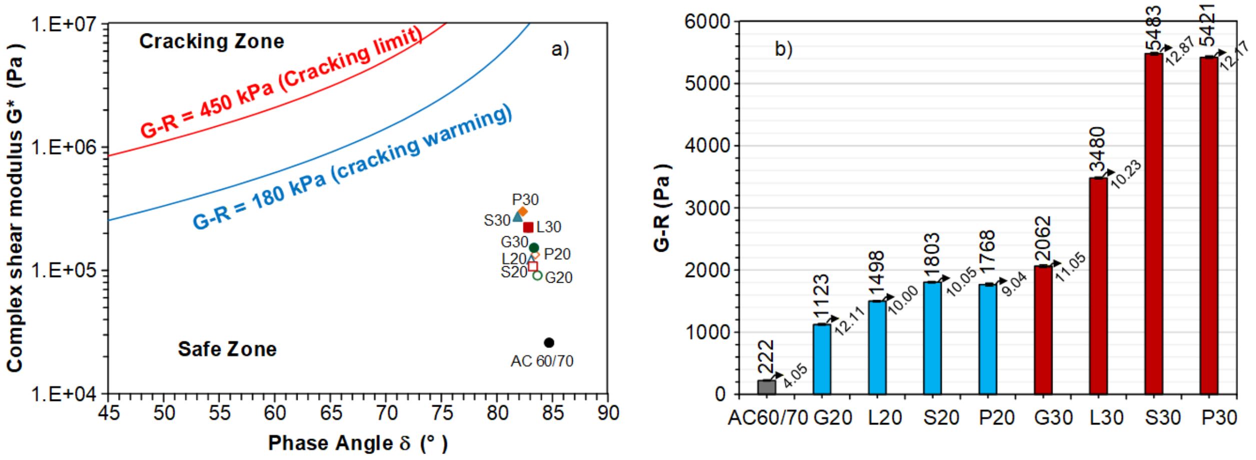

Figure 18. Cracking susceptibility: (a) Black space diagram; (b) G–R values

4. Conclusions and Recommendations

This study presents a comprehensive evaluation of shale and pumice as alternative mineral fillers in asphalt mastics, integrating physical, mineralogical (XRD), morphological (SEM), and rheological characterization. The results demonstrate that mineral fillers influence mastic behavior through filler-specific reinforcement mechanisms governed by the interplay between mineralogical composition, surface characteristics, and morphology, rather than simple volumetric stiffening.

XRD analysis revealed that pumice is composed predominantly of amorphous volcanic glass, which creates extensive internal porosity (SSA = 59.18 m^2/g) and abundant reactive surface sites. This mineralogy drives rutting-dominant modification: the highest complex modulus enhancement (7.3–9.4 times at 30% F/A), lowest Jnr (98.53% reduction), but shortest fatigue life (Nf,5% = 29,300 cycles at 20% F/A). In contrast, shale's quartz–kaolinite composition creates a layered morphology where the clay mineral's sheet structure enables microscale stress relaxation. This produces balanced rheological response: the longest fatigue life (Nf,5% = 45,200 cycles at 20% F/A) with meaningful rutting improvement (Jnr reduction of 93.32% at 30% F/A). Granite's crystalline quartz–albite framework and limestone's calcite-dominant mineralogy showed intermediate behavior consistent with their respective surface properties.

These findings establish a mineralogy–morphology–performance framework that supports performance-based filler selection. Pumice is effective for high-temperature environments where rutting dominates, while shale offers balanced performance for moderate climates with thermal cycling. Both can be sourced locally in Thailand as sustainable alternatives. Future research should investigate aging effects on mineralogy-specific reinforcement mechanisms, validate at mixture scale, and perform formal statistical analysis with intermediate filler contents.

5. Declarations

5.1. Author Contributions

Conceptualization, S.C. and P.C.; methodology, S.C. and P.C.; investigation, S.C.; resources, M.H.; validation, S.C. and P.C.; visualization, S.C.; writing—original draft preparation, S.C.; writing—review and editing, P.C.; supervision, P.C. All authors have read and agreed to the published version of the manuscript.

5.2. Data Availability Statement

The data presented in this study are available on request from the corresponding author.

5.3. Funding and Acknowledgments

This work was financially supported by King Mongkut's Institute of Technology Ladkrabang [2566-02-01-062]. We sincerely appreciate Tipco Asphalt Public Company Limited for providing the necessary facilities and equipment throughout the testing process.

5.4. Conflicts of Interest

The authors declare no conflict of interest.

6. References

[1] Huang, B., Shu, X., & Chen, X. (2007). Effects of mineral fillers on hot-mix asphalt laboratory-measured properties. International Journal of Pavement Engineering, 8(1), 1–9. doi:10.1080/10298430600819170.

[2] Chen, J. S., Kuo, P. H., Lin, P. S., Huang, C. C., & Lin, K. Y. (2008). Experimental and theoretical characterization of the engineering behavior of bitumen mixed with mineral filler. Materials and Structures/Materiaux et Constructions, 41(6), 1015–1024. doi:10.1617/s11527-007-9302-5.

[3] Wu, S., Zhu, J., Zhong, J., & Wang, D. (2011). Experimental investigation on related properties of asphalt mastic containing recycled red brick powder. Construction and Building Materials, 25(6), 2883–2887. doi:10.1016/j.conbuildmat.2010.12.040.

[4] Xing, B., Fang, C., Zhuang, C., Lyu, Y., & Fan, W. (2023). Mineral filler property and its influence on mastic interfacial cohesive behavior at low temperatures. Construction and Building Materials, 364, 129900. doi:10.1016/j.conbuildmat.2022.129900.

[5] Xing, B., Du, Y., Fang, C., Sun, H., Lyu, Y., & Fan, W. (2022). Particle morphology of mineral filler and its effects on the asphalt binder-filler interfacial interaction. Construction and Building Materials, 321, 126292. doi:10.1016/j.conbuildmat.2021.126292.

[6] Cheng, Y., Tao, J., Jiao, Y., Tan, G., Guo, Q., Wang, S., & Ni, P. (2016). Influence of the properties of filler on high and medium temperature performances of asphalt mastic. Construction and Building Materials, 118, 268–275. doi:10.1016/j.conbuildmat.2016.05.041.

[7] Guo, M., Tan, Y., Wang, L., & Wang, Y. (2017). Improvement of evaluation indicator of interfacial interaction between asphalt binder and mineral fillers. Construction and Building Materials, 151, 236–245. doi:10.1016/j.conbuildmat.2017.05.003.

[8] Chen, Y., Zheng, W., Xu, S., Tebaldi, G., & Su, Y. M. (2022). Characteristics of mineral fillers and their effects on mastic fracture resistance at intermediate temperature 20°C. Construction and Building Materials, 323, 126568. doi:10.1016/j.conbuildmat.2022.126568.

[9] Guo, M., Bhasin, A., & Tan, Y. (2017). Effect of mineral fillers adsorption on rheological and chemical properties of asphalt binder. Construction and Building Materials, 141, 152–159. doi:10.1016/j.conbuildmat.2017.02.051.

[10] Mukhtar, N., Mohd Hasan, M. R., Mohd Ghazali, M. F. H., Mohd Zin, Z., Shariff, K. A., & Sani, A. (2021). Influence of concentration and packing of filler particles on the stiffening effect and shearing behaviour of asphalt mastic. Construction and Building Materials, 295, 123660. doi:10.1016/j.conbuildmat.2021.123660.

[11] Zhao, Z., Wu, S., Liu, Q., Xie, J., Yang, C., Wan, P., Guo, S., & Ma, W. (2021). Characteristics of calcareous sand filler and its influence on physical and rheological properties of asphalt mastic. Construction and Building Materials, 301, 124112. doi:10.1016/j.conbuildmat.2021.124112.

[12] Muniandy, R., Aburkaba, E., & Taha, R. (2013). Effect of mineral filler type and particle size on the engineering properties of stone mastic asphalt pavements. Journal of Engineering Research, 10(2), 13–32. doi:10.24200/tjer.vol10iss2pp13-32.

[13] Tan, Y., & Guo, M. (2014). Interfacial thickness and interaction between asphalt and mineral fillers. Materials and Structures/Materiaux et Constructions, 47(4), 605–614. doi:10.1617/s11527-013-0083-8.

[14] Zhang, J., Li, X., Liu, G., & Pei, J. (2019). Effects of material characteristics on asphalt and filler interaction ability. International Journal of Pavement Engineering, 20(8), 928–937. doi:10.1080/10298436.2017.1366765.

[15] Ramli, H., Zainal, N. F. A., Hess, M., & Chan, C. H. (2022). Basic principle and good practices of rheology for polymers for teachers and beginners. Chemistry Teacher International, 4(4), 307–326. doi:10.1515/cti-2022-0010.

[16] Mukhtar, N., Mohd Hasan, M. R., Osman, H., Mohd Zin, Z., Shariff, K. A., Nur, N. I., & Sani, A. (2023). Rheological and physicochemical characteristics of asphalt mastics incorporating lime kiln dust and dolomite powder as sustainable fillers. Journal of Road Engineering, 3(1), 98–112. doi:10.1016/j.jreng.2023.01.001.

[17] Bi, Y., Wei, R., Li, R., Zhang, J., & Pei, J. (2020). Evaluation of rheological master curves of asphalt mastics and asphalt-filler interaction indices. Construction and Building Materials, 265, 120046. doi:10.1016/j.conbuildmat.2020.120046.

[18] Zhang, Q., Luo, J., Yang, Z., Wang, J., Zhao, Y., & Zhang, Y. (2023). Creep and fatigue properties of asphalt mastic with steel slag powder filler. Case Studies in Construction Materials, 18, 1743. doi:10.1016/j.cscm.2022.e01743.

[19] Li, H., Wang, W., Li, W., Taoum, A., Zhao, G., & Guo, P. (2019). Replacement of Limestone with Volcanic Stone in Asphalt Mastic Used for Road Pavement. Arabian Journal for Science and Engineering, 44(10), 8629–8644. doi:10.1007/s13369-019-04028-w.

[20] Underwood, B. S. (2016). A continuum damage model for asphalt cement and asphalt mastic fatigue. International Journal of Fatigue, 82, 387–401. doi:10.1016/j.ijfatigue.2015.08.020.

[21] Chaudhary, M., Saboo, N., Gupta, A., & Miljković, M. (2022). Contribution of mineral filler to the fatigue damage behaviour of bituminous mastic. Construction and Building Materials, 334, 127120. doi:10.1016/j.conbuildmat.2022.127120.

[22] Wang, W., Cheng, Y., Tan, G., Liu, Z., & Shi, C. (2018). Laboratory investigation on high- and low-temperature performances of asphalt mastics modified by waste oil shale ash. Journal of Material Cycles and Waste Management, 20(3), 1710–1723. doi:10.1007/s10163-018-0737-2.

[23] Zhang, J., Shen, Q., Ji, P., Wang, J., & Xiao, Y. (2023). Influence of filler type and rheological properties of asphalt mastic on the asphalt mastic–aggregate interaction. Materials, 16(2), 574. doi:10.3390/ma16020574.

[24] Terzi, S., & Büyükdoğaç, E. M. (2018). Evaluation of Zeolite and Pumice Waste As Mineral Aggregate and Filler for Producing Lightweight Asphalt Concrete Mixtures. Mühendislik Bilimleri ve Tasarım Dergisi, 6(1), 118–123. doi:10.21923/jesd.311826.

[25] Koyuncu, M., Ulay, G., & Şeker, U. (2023). Effect of Pumice Powder on Mechanical, Thermal, and Water Absorption Properties of Fiberboard Composites. Fibres and Textiles in Eastern Europe, 31(3), 30–36. doi:10.2478/ftee-2023-0025.

[26] Bagampadde, U., Kaddu, D., & Kiggundu, B. M. (2013). Evaluation of rheology and moisture susceptibility of asphalt mixtures modified with low density polyethylene. International Journal of Pavement Research and Technology, 6(3), 217–224. doi:10.6135/ijprt.org.tw/2013.6(3).217.

[27] Celik, S., Family, R., & Menguc, M. P. (2016). Analysis of perlite and pumice based building insulation materials. Journal of Building Engineering, 6, 105–111. doi:10.1016/j.jobe.2016.02.015.

[28] Nazary, M., & Kofteci, S. (2018). Effect of filler types and asphalt penetration grade on properties of asphalt mastic. Petroleum Science and Technology, 36(18), 1503–1509. doi:10.1080/10916466.2018.1501385.

[29] Aslan, Ş., & Aktaş, B. (2019). Use of diatomite and pumice as stabilizers in stone mastic asphalt mixtures. Revista de La Construccion, 17(3), 531–541. doi:10.7764/RDLC.17.3.531.

[30] Kofteci, S. (2018). Investigation on the usability of pumice as fibre in stone mastic asphalt. Gradjevinar, 70(8), 695–701. doi:10.14256/JCE.2310.2017.

[31] Hamedi, G. H., & Esmaeeli, M. R. (2017). Mechanical Properties of Open Graded Asphalt Mixtures with Pumice Aggregate. AUT Journal of Civil Engineering, 1(2), 189-194. doi:10.22060/ceej.2017.13383.5396.

[32] Zhang, L., Xiao, D., Lu, S., Jiang, S., & Lu, S. (2019). Effect of sedimentary environment on the formation of organic-rich marine shale: Insights from major/trace elements and shale composition. International Journal of Coal Geology, 204, 34–50. doi:10.1016/j.coal.2019.01.014.

[33] Buriyev, S., Davranov, S., Kuchkarov, Y., & Saydakberova, I. (2021). The effect of shale mineral powder on the strength of asphalt concrete. E3S Web of Conferences, 264, 2052. doi:10.1051/e3sconf/202126402052.

[34] Meena, P., Naga, G. R. R., Kumar, P., & Monu, K. (2024). Effect of Mechanical Properties of Cold Mix Asphalt Mixture Containing Different Proportion of Fillers. International Journal of Pavement Research and Technology, 17(4), 982–998. doi:10.1007/s42947-023-00281-3.

[35] Xing, B., Fan, W., Zhuang, C., Qian, C., & Lv, X. (2019). Effects of the morphological characteristics of mineral powder fillers on the rheological properties of asphalt mastics at high and medium temperatures. Powder Technology, 348, 33–42. doi:10.1016/j.powtec.2019.03.014.

[36] Davis, C., & Castorena, C. (2015). Implications of physico-chemical interactions in asphalt mastics on asphalt microstructure. Construction and Building Materials, 94, 83–89. doi:10.1016/j.conbuildmat.2015.06.026.

[37] Nobakht, M., & Sakhaeifar, M. S. (2018). Dynamic modulus and phase angle prediction of laboratory aged asphalt mixtures. Construction and Building Materials, 190, 740–751. doi:10.1016/j.conbuildmat.2018.09.160.

[38] Nur, N. I., Chailleux, E., & Airey, G. D. (2011). A comparative study of the influence of shift factor equations on master curve construction. International Journal of Pavement Research and Technology, 4(6), 324–336.

[39] AASHTO TP 101‐14. (2014). Standard method of test for estimating damage tolerance of asphalt binders using the linear amplitude sweep. American Association of State Highway and Transportation Officials, Washington, D.C., United States.

[40] Menapace, I., Garcia Cucalon, L., Kaseer, F., Arámbula-Mercado, E., Epps Martin, A., Masad, E., & King, G. (2018). Effect of recycling agents in recycled asphalt binders observed with microstructural and rheological tests. Construction and Building Materials, 158, 61–74. doi:10.1016/j.conbuildmat.2017.10.017.

[41] Guan, M., Guo, M., Tan, Y., & Du, X. (2023). Study on the effect of aging on cracking resistance of virgin asphalt binder and its evolution model. Construction and Building Materials, 407, 133443. doi:10.1016/j.conbuildmat.2023.133443.

[42] Li, F., & Yang, Y. (2020). Understanding the temperature and loading frequency effects on physicochemical interaction ability between mineral filler and asphalt binder using molecular dynamic simulation and rheological experiments. Construction and Building Materials, 244, 118311. doi:10.1016/j.conbuildmat.2020.118311.

[43] Cui, Y., Si, C., Li, S., Jia, Y., & Guo, B. (2024). Iron Tailings as Mineral Fillers and Their Effect on the Fatigue Performance of Asphalt Mastic. Materials, 17(12), 2927. doi:10.3390/ma17122927.

[44] Grabowski, W., & Wilanowicz, J. (2008). The structure of mineral fillers and their stiffening properties in filler-bitumen mastics. Materials and Structures/Materiaux et Constructions, 41(4), 793–804. doi:10.1617/s11527-007-9283-4.